Walker-like Domain Wall breakdown in layered Antiferromagnets driven by staggered spin-orbit fields

Supplementary Note 1

We revisit here the concept of the so-called gyrofield to explain the physical origin of the vortex core reversal in submicron-sized dots [1]. We extend its treatment to 1D systems and to purely translational motion. Hence, associated to DW_1, driven by SO-field, emerges a magnetic field whose origin is due the translational dynamics of the DW itself. The kinetic part of the Lagrangian density can be written in the invariant form as [1-3]

$$\mathcal{L}_{\rm kin}(\mathbf{m},\dot{\mathbf{m}}) = \frac{M_{\rm s}}{\gamma}\frac{\mathbf{n}\cdot(\mathbf{m}\times\dot{\mathbf{m}})}{1+\mathbf{m}\cdot\mathbf{n}}, \tag{1}$$

where $\mathbf{m}=\mathbf{M}/M_{\rm s}$ is the reduced magnetization, and $\mathbf{n}$ is a unit vector along an arbitrary direction called as the Dirac´s string, γ is the gyroscopic constant and $\dot{\mathbf{m}}=\partial_t\mathbf{m}$.

In the following, we calculate the kinetic field for a Néel domain wall moving along the $\mathbf{x}$-axis due to the action of a spin-orbit field directed along the $\mathbf{y}$-axis. It was suggested by Guslienko et al. [1] to re-write the kinetic Lagrangian (Eq. 1) in the form of the effective Zeeman energy

$$\mathcal{L}_{\rm kin} = M_{\rm s}\mathbf{m}\cdot\mathbf{h}, \tag{2}$$

where an effective magnetic field $\mathbf{h}$ (gyrofield or kinetic field) proportional to the magnetisation derivative with respect to time $\dot{\mathbf{m}}$ was introduced as

$$\mathbf{h} = \frac{1}{\gamma}\frac{1}{(1+\mathbf{n}\cdot\mathbf{m})^2}\left[-\mathbf{m}\times\dot{\mathbf{m}} + (\dot{\mathbf{m}}\times\mathbf{n})(1+\mathbf{n}\cdot\mathbf{m})\right]. \tag{3}$$

Note that only longitudinal component of the gyrofield along the $\mathbf{n}$ direction (the first term in Eq. (3)) was used in [1] to describe critical velocity of the vortex core motion to reach the vortex core polarization reversal. The longitudinal component of the gyrofield satisfies the usual relation of the energy density and corresponding effective field

$$h_n = \frac{1}{M_{\rm s}}\frac{\delta\mathcal{L}_{\rm kin}}{\delta m_n}, \tag{4}$$

whereas for the transverse gyrofield components (perpendicular to the $\mathbf{n}$ direction) the relation

$$\mathbf{h}_t = \frac{1}{2M_{\rm s}}\frac{\delta\mathcal{L}_{\rm kin}}{\delta\mathbf{m}_t} \tag{5}$$

is valid. The variation derivatives with respect to $\mathbf{m}$, $\dot{\mathbf{m}}$ dynamical variables are used in Eqs. (4), (5).

The $\mathbf{n}$ direction was chosen along the cylindrical dot axis Oz (vortex core magnetisation direction). In the case of a domain wall dynamics and parametrisation of the magnetisation via the spherical angles $\mathbf{m}(\theta,\phi)$ it seems that $\mathbf{n}$ can be defined as direction of the z-axis of the spherical coordinate system. Note that the kinetic field given by Eq. 3 is related to neither the magnetic emergent field nor electric emergent field which are often introduced to describe the dynamics of magnetisation textures (vortices, skyrmions, domain walls etc.). See, for instance [4]. Nevertheless, the concept of the kinetic field is useful to describe qualitatively the dynamics of the magnetisation textures because it is proportional to the texture velocity and can be used as a fictitious driving force for the magnetisation texture dynamic deformations.

The **z**-component of the kinetic field is found to reach values up to 35 T in absolute value, the **x** and **y** components reach a maximum absolute value of circa 6 mT and 3.5 mT respectively, see Supplementary Figure 1. Such big difference between the kinetic field in-plane and out-of-plane components is due to specific magnetization texture considered. The domain wall magnetisation is in the basal xOy plane and $m_z = 0$ approximately.

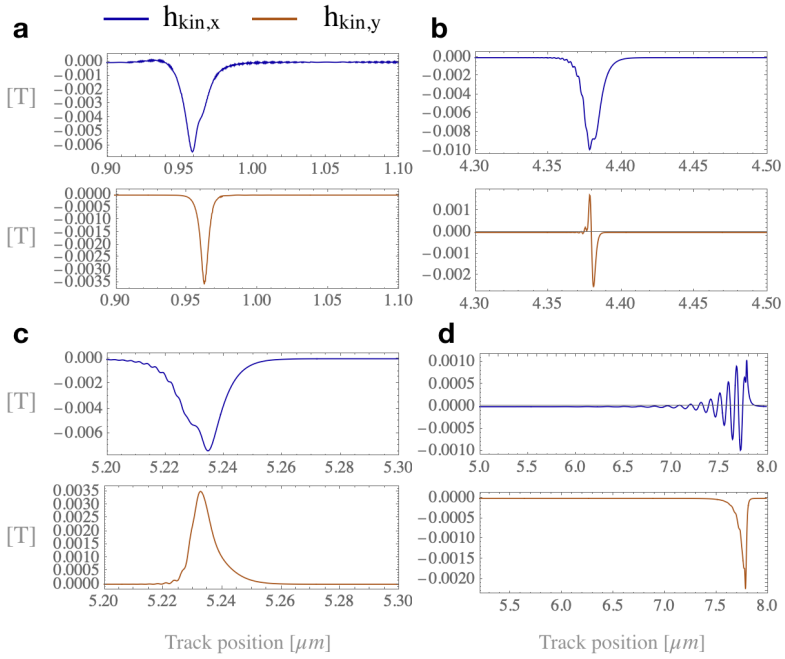

Supplementary Figure 1: Snapshots of x and y-components of the kinetic field at different instances during DW_1 motion along the track. Panel **a** to **d** corresponds to physical times of 10, 90, 110 and 145 picoseconds.

The region generated in front of the DW_1 that is fully reversed along the $-m_x$ direction (see Supplementary Figure 2) is about 20 nm in the moving frame. In the rest frame this length corresponds to more than twice the exchange length, l_{ex} defined as: $l_{\text{ex}} = (A/K_{\text{ani}})^{1/2}$=19.78 nm, where A and $K_{2\parallel}$ represent the effective exchange stiffness and uniaxial anisotropy constants respectively (see Table 1 in the main text). Once this occurs, the energy competition between the anisotropy energy and the exchange energy over the region which is twice l_{ex} led to a formation of domains walls preserving the overall winding number. We note that the crucial point is not just the DW_1 to reach certain speed to generate a large enough kinetic fields but also that the kinetic field extends sufficiently in space to accommodate a DW-pair.

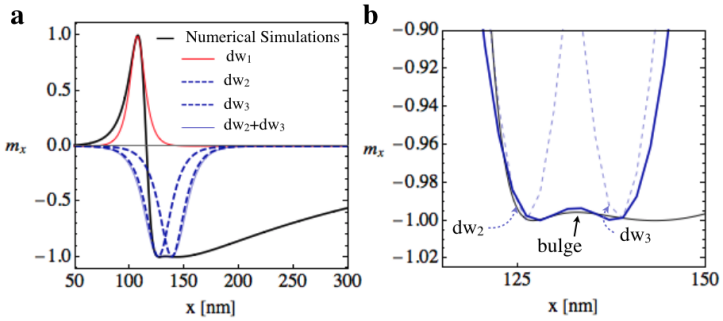

Supplementary Figure 2: **a** m_x distribution along the track. We have over imposed a domain wall profile (black solid line) given by Eq. 5 to extract the DW_1 width as well as profiles for DW_2 and DW_3. **b** Zoom-in on the region where for the first time we observe a small bulge that suggest the nucleation of DW_2 and DW_3 is about to begin. We have again super imposed a profile comprised by DW_2 and DW_3 (dashed blue lines) in order to reproduce in the best manner the small bulge. The domain wall widths extracted from the fitting for DW_2 and DW_3 are: Δ_{DW_2}=Δ_{DW_3}=10 nm.

Different type of magnetic distributions could in principle appear obeying the boundary conditions imposed over the generated magnetic domain, see Supplementary Figure 3 **a**. Supplementary Figure 3 panel **b** shows an arrangement where the Zeeman energy comprised by the spin-orbit field and the kinetic field are minimised. Moreover, one can differentiate two magnetic textures whose winding number w, are opposite giving an overall winding number cero and therefore preserving the overall topological charge. Panel **c** in Supplementary Figure 3 shows that although that particular arrangement minimises the spin-orbit part of the Zeeman energy, it is not compatible with the orientation of the spins promoted by the torque exerted by the kinetic field (along negative $\hat{x}$.dir.) nor the Zeeman energy from the kinetic field.

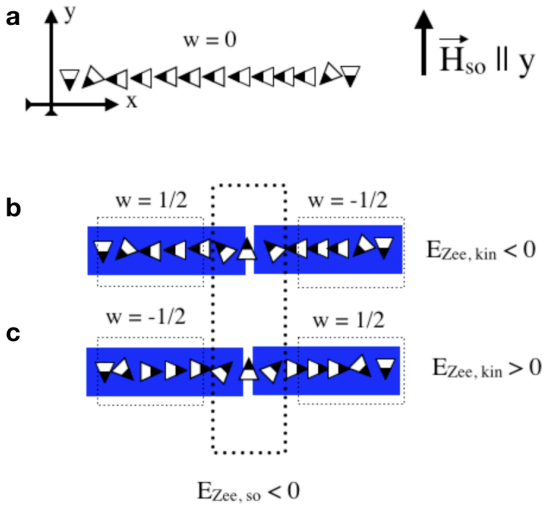

Supplementary Figure 3: **a** Schematic of the coordinate system and the orientation of the spin-orbit field $\vec{H}_{so}$. Panels **b** - **c** corresponds to the possible arrangements compatible with the spin-orbit field but only the texture shown in **b** correspond to appropriate arrangement consistent with the torque exerted by the z-component of the kinetic field as well as the the minimisation of the Zeeman energy coming from the kinetic field and the SO-field.

Supplementary Note 2

The topological charge distribution extracted from the numerical simulations corresponds to: $|\ \mathrm{DW}_1, \mathrm{DW}_2, \mathrm{DW}_3\rangle = |\ \frac{1}{2}, \frac{1}{2}, -\frac{1}{2}\rangle$ where the numbers within the bracket represent the winding number associated to each DW_i. As DW_1 and DW_2 have the same topological charge implies that the central spin of each of them are antiparallel oriented with respect to each other (as shown in Supplementary Figure 4) which implies that, as they are located in the same ferromagnetic basal plane, the exchange interaction among them will be therefore repulsive.

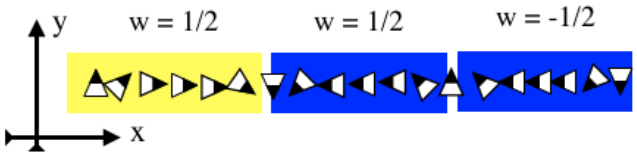

Supplementary Figure 4: Illustration of the magnetisation distribution after the nucleation process has been completed. This assortment as shown before is the only compatible with the conditions of the numerical simulations and will be our starting point for explaining the boost experienced by the DW_3

In the following, we calculate the exchange interaction between DW_1 and DW_2 as a function of the distance between them. The azimuthal angle of a 1D domain wall is described by

$$\Phi\left(x,t\right) = 2\arctan\left[\mathrm{Exp}\left[q\frac{(x-X(t))}{\Delta(t)}\right]\right], \tag{6}$$

where $X(t)$ represents the domain wall position, $\Delta(t)$ the domain wall width and q the topological charge. Note that even though the domain wall is treated as a rigid object is subject to contraction and so Δ has an explicit dependence on time, t. For sake simplicity, we assume two domain walls with the same width and same topological charges so that $q_{1,2} = q = +1$. Therefore the compound profile of the two magnetic domain wall will simply be the superposition of both profiles

$$\Phi\left(x\right) = 2\arctan\left[\exp\left[q\frac{(x-X_1(t))}{\Delta(t)}\right]\right] + 2\arctan\left[\exp\left[q\frac{(x-X_2(t))}{\Delta(t)}\right]\right], \tag{7}$$

The exchange interaction E_{exc}, is given by

$$E_{\mathrm{exc}} = A\int_{-\infty}^{+\infty}\left(\sum_i \partial_x\Phi_i\right)^2 dx, \tag{8}$$

where the integral is calculated over the whole 1-dimensional chain. For a single domain wall the spatial derivative of the azimuthal angle is given by

$$\partial_x\Phi_i = \frac{q}{\Delta(t)}\,\mathrm{sech}\left(q\frac{(x-X_i(t))}{\Delta(t)}\right). \tag{9}$$

Hence, the overall exchange interaction composed by the two magnetic textures is

$$\sum_i \partial_x\Phi_i = \frac{1}{\Delta(t)}\left[\mathrm{sech}\left(\frac{x-X_1(t)}{\Delta(t)}\right) + \mathrm{sech}\left(\frac{x-X_2(t)}{\Delta(t)}\right)\right]. \tag{10}$$

Now just taking the square in Eq. 9 allows us to calculate the exchange interaction

$$\left(\sum_i \partial_x \Phi_i\right)^2 = \frac{1}{\Delta(t)^2}\left[\operatorname{sech}^2\left(\frac{x-X_1(t)}{\Delta(t)}\right) + \operatorname{sech}^2\left(\frac{x-X_2(t)}{\Delta(t)}\right) + 2\operatorname{sech}\left(\frac{x-X_1(t)}{\Delta(t)}\right)\operatorname{sech}\left(\frac{x-X_2(t)}{\Delta(t)}\right)\right], \tag{11}$$

where we can identify the first two terms as the self-exchange energy terms for each of the domain walls

$$E_i = \frac{A}{\Delta(t)^2}\int_{-\infty}^{+\infty} \operatorname{sech}^2\left(\frac{x-X_i(t)}{\Delta(t)}\right) \mathrm{d}x. \tag{12}$$

Whereas the third term in Eq. 10 corresponds to the interaction between the domain walls.

$$E_{12} = \frac{2A}{\Delta(t)^2}\int_{-\infty}^{+\infty} \operatorname{sech}\left(\frac{x-X_1(t)}{\Delta(t)}\right)\operatorname{sech}\left(\frac{x-X_2(t)}{\Delta(t)}\right) \mathrm{d}x. \tag{13}$$

It is possible to rewrite Eq. (11) as

$$E_{\text{exc}} = E_1 + E_2 + E_{12}. \tag{14}$$

In order to calculate the interaction term, E_{12}, given by Eq. 12, we make use of hyperbolic functions and the following tabulated trigonometric relationship

$$\cosh(\xi_1)\cosh(\xi_2) = a + a\cosh(2\xi_1) + c\sinh(2\xi_1), \tag{15}$$

where $\xi_i = (x - X_i(t))/\Delta(t)$, and the coefficients a and c are defined as

$$a = \frac{1}{2}\cosh\left(\frac{X_1(t)-X_2(t)}{\Delta(t)}\right), \tag{16}$$

$$c = \frac{1}{2}\sinh\left(\frac{X_1(t)-X_2(t)}{\Delta}\right). \tag{17}$$

The integral in Eq. 12 can be now expressed as

$$E_{12} = \frac{2A}{\Delta^2}\int_{-\infty}^{+\infty} \frac{\mathrm{d}x}{a + a\cosh(2\xi_1) + c\sinh(2\xi_1)} = \frac{2A}{\Delta^2} I, \tag{18}$$

where I is the sum of the two following integrals

$$I = \frac{\Delta(t)}{2}\left[\int_0^{+\infty} \frac{\mathrm{d}y}{a + a\cosh(y) + c\sinh(y)} + \int_0^{+\infty} \frac{\mathrm{d}y}{a + a\cosh(y) - c\sinh(y)}\right] =$$

$$\frac{\Delta}{2}\left[I(a,a,c) + I(a,a,-c)\right]. \tag{19}$$

The solution of this integral can be found in [5] and is given by

$$I(a,a,c) = \frac{1}{c}\ln\left(\frac{a+c}{a}\right). \tag{20}$$

Now, $2\,\mathrm{atanh}\,(x) = \ln\left[(1+x)\,/\,(1-x)\right]$ and the integral for I can be rewritten as

$$I = 2\,(X_1(t) - X_2(t))\,\mathrm{csch}\left(\frac{X_1(t) - X_2(t)}{\Delta(t)}\right), \tag{21}$$

and, subsequently, Eq. 12 can be expressed as

$$E_{12} = q_1 \cdot q_2 \cdot \frac{4A\,(X_1(t) - X_2(t))}{\Delta(t)^2}\,\mathrm{csch}\left(\frac{X_1(t) - X_2(t)}{\Delta(t)}\right), \tag{22}$$

where the product of the DW topological charges $q_1 \cdot q_2$=+1 corresponds to repulsion, and $q_1 \cdot q_2$= -1 to attraction of DWs.

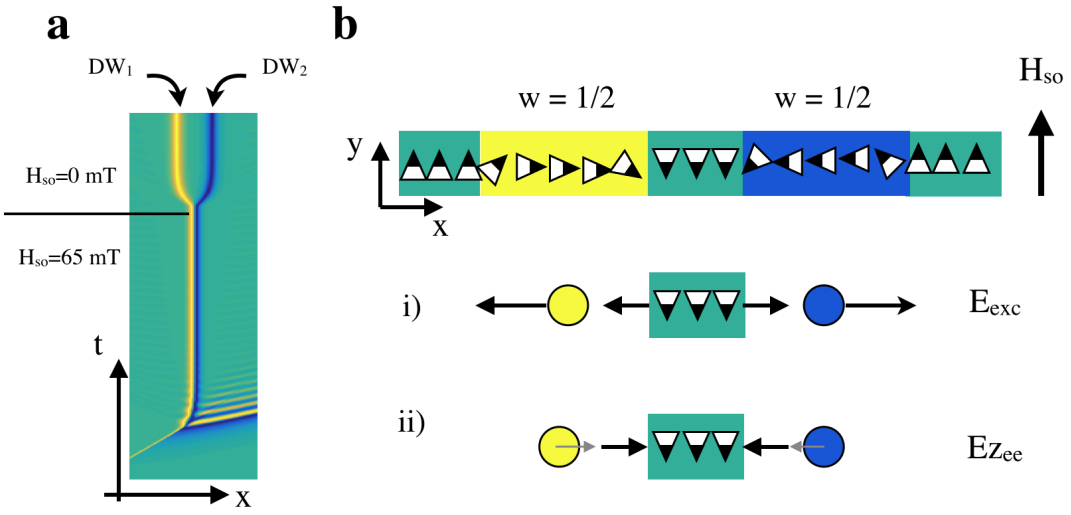

Supplementary Figure 5: **a** Temporal evolution of DW_1 and DW_2 after the nucleation. The two domain walls are separated by a distance that will be kept constant. When the spin-orbit field is set to zero the two domain walls separate even further. **b** Schematic illustration of the role played by the exchange energy and the Zeeman energy. While the exchange energy tries to separate DW_1 and DW_2, the Zeeman energy forces them to stay as close as possible.

Once the nucleation process has terminated there is a stable distance between DW_1 and DW_2 as shown in Supplementary Figure 5 **a**. Moreover, we can observed that this distance increases when the spin-orbit field is set to zero. Supplementary Figure 5 **b** shows an illustration of the magnetisation distribution. We can see that the two domain walls (DW_1 and DW_2) have same winding number and as a consequence, it appears a region in between them whose polarisation is along the $-\hat{y}$-direction. Sub-panel i) in Supplementary Figure 5 **b** shows that the repulsive interaction between DW_1 and DW_2 due to the exchange interaction, E_{exc}, results into an expansion of the magnetic domain separating both domain walls. On the contrary, ii) sub-panel shows that as the magnetic domain between the domain walls has opposite orientation with respect the spin-orbit field, H_{so}, the Zeeman energy, E_{Zee}, tries to shrink the magnetic domain in order to minimise the Zeeman energy and as a result the two domain walls are pulled together. Overall, we can see that the stable distance among the two domain walls is due to the competition between the exchange and Zeeman energies. This competition can be expressed as

$$\Delta E = (X_1 - X_2)M_{\mathrm{s}}H_{\mathrm{so}} + \frac{4A\,(X_1 - X_2)}{\Delta^2}\,\mathrm{csch}\left(\frac{X_1 - X_2}{\Delta}\right), \tag{23}$$

where as before X_1 and X_2 represent the location of the domain walls' center, Δ is the domain wall width (see Supplementary Figure 2) for each domain walls extracted from the numerical simulations.

Supplementary Figure 6 **a** shows the different energies in action for a spin-orbit field of 20 mT. As the the spin-orbit field and magnetic domain between the two domain walls is antiparallel, the minimum energy corresponds to a zero distance between the walls. The opposite happens with the exchange energy, the smaller is the distance between the two domain walls the larger is the exchange energy ($A > 0$). One can see that (brown dashed line) that when combing the exchange and the Zeeman energy appears a global minimum which corresponds to a stable configuration distance between DW_1 and DW_2. The stable distance between the two domain walls as a function of the applied spin-orbit field is represented in Supplementary Figure 6 **b**. It can be observed that starting for the larger spin-orbit field (60 mT), the stable distance increases as the spin-orbit field (SO-field) decrease meaning that the Zeeman force needs more extension of the magnetic domain to compensate the repulsion between the domain walls.

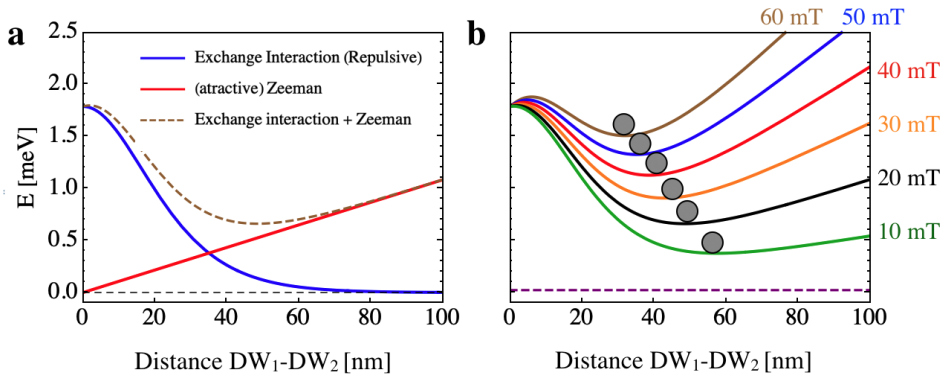

Supplementary Figure 6: **a** Exchange and Zeeman energy as a function of the DW_1 to DW_2 distance for an applied spin-orbit field of 20 mT. **b** Total energy comprised by the exchange energy and Zeeman energy for different applied spin-orbit fields. The small grey dots represent the global minimum for the different spin-orbit fields and the dashed purple line represents the thermal energy ($k_B T$) at room temperature.

Supplementary Note 3

As the nucleation occurs while DW_1 translates, we assume that the dip which will eventually led to the DW-pair, DW_2 and DW_3 is also propagating at the same velocity as DW_1. The DW_1 mobility depends linearly on the SO-field as follows

$$v_{\mathrm{DW}_1} = \frac{\gamma}{\alpha} H_{\mathrm{so}}\, \Delta_0 \left[1 - \left(\frac{v_{\mathrm{DW}_1}}{v_{\mathrm{g}}}\right)^2\right]^{1/2}, \tag{24}$$

where α is the damping constant, γ is the gyromagnetic ratio, H_{so} is the spin-orbit field, Δ_0 is the DW-width at rest and v_{g} is the maximum group velocity of the magnons. The sole energies involved in the dynamics of DW_3 are: the Zeeman energy (coming from the spin-orbit field) and the exchange interaction between DW_1 and DW_2 which we assume that is transferred to DW_3. The repulsive exchange energy between DW_1 and DW_2 is given by

$$\mathcal{E}_{\mathrm{exc}} = \frac{4A\left(X_p(t_0) - X_1(t_0)\right)}{\Delta^2_{\mathrm{DW}}(t_0)}\, \mathrm{csch}\left(\frac{X_p(t_0) - X_1(t_0)}{\Delta_{\mathrm{DW}}(t_0)}\right), \tag{25}$$

where $X_p(t_0) - X_1(t_0)$ is the distance between DW_1 and DW-pair, Δ_{DW} is the domain wall width extracted from the simulations. A is the effective ferromagnetic exchange stiffness. For sake of

simplicity, we translate our system of reference to DW_1 which implies $X_1(t_0) = 0$ and therefore $X_p(t_0) - X_1(t_0) = x(t_0)$. We obtain the DW_3 width by fitting two domain walls to the dip in front of the moving DW_1 as shown in Supplementary Figure 2 **b**.

The Lagrangian formalism allows us to characterise the DW_3 boost as a function of its distance to the DW_2. By integrating over the Lagrangian density, $\mathcal{L}$, for the magnetisation profile of the Néel wall in an embedded ferromagnetic plane, we obtain the temporal evolution of each canonical coordinate,

$$\frac{d}{dt}\frac{\partial \mathcal{L}}{\partial \dot{\xi}} - \frac{\partial \mathcal{L}}{\partial \xi} = F_\xi, \tag{26}$$

where F_ξ makes reference to non-conservative forces and can be calculate by the so-called Rayleigh dissipation function, W

$$F_\xi = -\frac{\partial W}{\partial \dot{\xi}} = -\frac{\alpha \mu_0 M_s}{2\gamma}\frac{\partial}{\partial \dot{\xi}}\int d^3r \left(\dot{\Phi}^2 + \dot{\Theta}^2 \sin^2\Phi\right), \tag{27}$$

where μ_0 is the magnetic permeability in vacuum and Φ and Θ represents the in-plane and out-of-plane component of the magnetisation. Here after, we assume that the values for the damping, saturation magnetisation, anisotropy constants and ferromagnetic exchange stiffness are the same for all the ferromagnetic layers that conform the Mn_2Au unit crystal.

By combining again the Rayleigh dissipation function and the Euler-Lagrange equation of motion allows us to get the boost over v_{DW_3} as a function of its distance to DW_1

$$v_{DW_3} = \frac{2\gamma A}{\alpha M_s \Delta_{DW_3}^2}\left[x(t_0)\coth\left(\frac{x(t_0)}{\Delta_{DW_3}(t_0)}\right) - \Delta_{DW_3}(t_0)\right]\operatorname{csch}\left(\frac{x(t_0)}{\Delta_{DW_3}(t)}\right). \tag{28}$$

However, the overall DW_3 speed will be comprised by its initial velocity provided by the DW_1 and the boost coming from the repulsion between DW_1 and DW_2 which can be expressed as

$$v_{DW_3} = \frac{\gamma}{\alpha}H_{so}\,\Delta_0\left[1-\left(\frac{v_{DW_1}}{v_g}\right)^2\right]^{1/2} + \frac{2\gamma A}{\alpha M_s \Delta_{DW_3}^2}\left[x(t_0)\coth\left(\frac{x(t_0)}{\Delta_{DW_3}(t_0)}\right) - \Delta_{DW_3}(t_0)\right]\operatorname{csch}\left(\frac{x(t_0)}{\Delta_{DW_3}(t_0)}\right). \tag{29}$$

Supplementary Figure 7 shows the dependence of the maximum speed experienced by DW_3 as a function of the distance between DW_3 and DW_1 according to Eq. 28. Note, the maximum boost does not correspond to a zero distance due to finite size of the DWs. Instead, the maximum boost in speed which corresponds to 133 km/s appears at a distance of 16.1 nm between the DW_1 and DW_3. From numerical simulations, the distance between the DW_1 and DW_2 is 17 nm and the extracted value for the speed about 177 km/s.

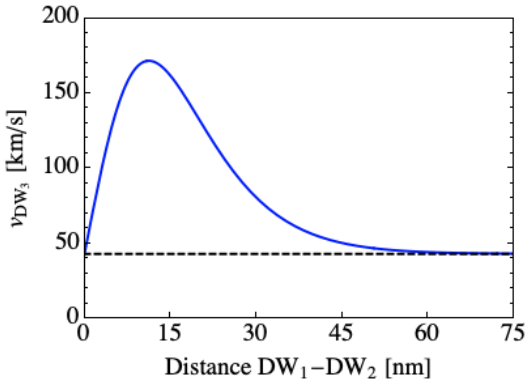

Supplementary Figure 7: Blue color line represents the DW_3 velocity as a function of the distance between DW_1 and DW_3. Dashed black line represents the maximum group velocity of the magnons, v_g.

Supplementary Note 4

A Mn_2Au spin lattice is used for the atomistic spin dynamics simulations. The structure is shown in Supplementary Figure 8. There are two types of sites occupied by Mn, A and B as indicated in the figure. A current density along unit-direction $\hat{\mathbf{j}}$ coinciding with the x-direction, results in a staggered magnetic field, $\mathbf{H}_{\mathrm{SO}}$ at each site (see Supplementary Figure 8).

We use 60000 unit Mn_2Au lattice cells in the simulations along x. Periodic boundary conditions (wrap-around) are applied along the y-direction. As initial condition for the dynamical simulations we use precomputed and stabilized 180° domain walls. Spins in the xy-plane are ferromagnetic ally ordered (the J_3-bonds) and antiferromagnetically coupled along z (the J_1 and J_2 -bonds) as also indicated in Supplementary Figure 8). Data is extracted along a 1D line shown by a dotted line in Supplementary Figure 8 denoted Data extraction line.

The LLG-equation is integrated using a 5th order Runge-Kutta scheme with adaptive time-stepping. The domain wall position is tracked from moments of the winding number density w along the data extraction line at each time t via $x_{\mathrm{DW}}(t) = \frac{\int xw(x,t)dx}{\int w(x,t)dx}$ from which the speed is computed. The time dependence of the DW width is computed by fitting the S_y-component along the data extraction line to $\phi(x,t) = 2\arctan\left[\exp\left(\frac{x-x_{C,t}}{\Delta_{\mathrm{DW}}(t)}\right)\right]$, in which $x_{C,t}$ is the DW centre and $\Delta_{\mathrm{DW}}(t)$ is the DW width. The fitted values will yield a slight overestimation of the actual width during acceleration and deceleration stages of the DW motion as the fitting function assumes a symmetric profile.

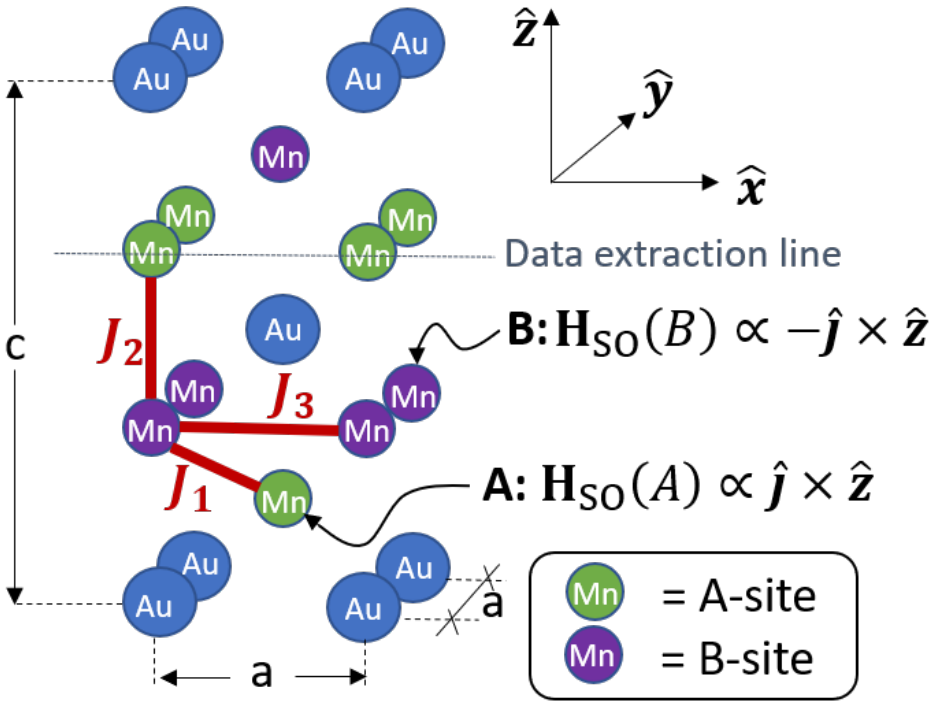

Supplementary Figure 8: Single Mn_2Au cell used in the simulations. Mn-spins occupy A and B-type sites resulting in a staggered distribution of $\mathbf{H}_{\mathrm{SO}}$ as indicated in this figure. The exchange bonds taken into consideration, J_1, J_2 and J_3 are shown by thick red lines. Note that the ferromagnetic J_3 bond acts between all nearest neighbour's in the xy-plane. Crystal dimensions are a=0.3328 nm and c = 0.8539 nm. The 1D line whereby spatio-temporal data is extracted from simulations is shown as a finely dotted line and denoted " Data extraction line ".

The maximum magnon group velocity v_g is estimated in a separate simulation according to the following steps: A homogeneous Néel state is used as starting state. Then spins within a local region in the centre are slightly perturbed by imposing small S_x-component. The symmetry of this perturbation is such that the induced S_x-components alternate in sign along the z-direction. Using the perturbed state as starting configuration, the system is let to ring down and the time dependence of S_x is recorded at each site on the data extraction line. In a last step, a 2D FFT is performed, giving frequency (f) versus k-vector along x (k_x). The (f, k_x) points with maximum oscillation-amplitudes is then extracted to form a line plot of the dispersion relation shown in Supplementary Figure 9.

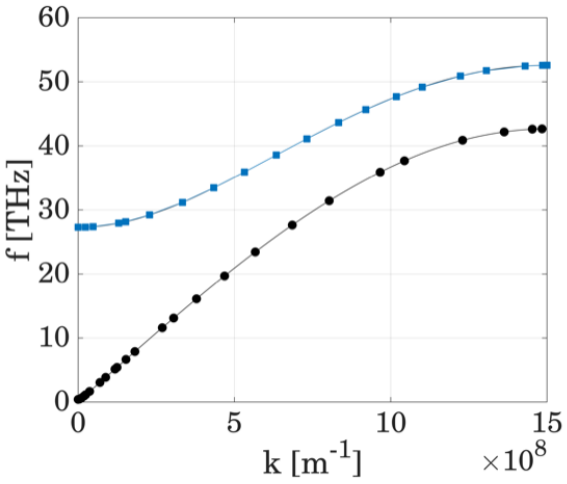

Supplementary Figure 9: Computed dispersion relation. The lower branch is used in the velocity vs. k-vector plot in the main text as it contains the highest slope and thus yields the maximum group velocity.

The maximum magnon group velocity v_g is extracted from the lower branch (black filled circles and black line in Supplementary Figure 9) by $v_g = \left(\frac{d\omega(k)}{dk}\right)_{max}$, where $\omega = 2\pi f$. The dispersion-relation will affected by the presence of a background SO-field present when the DW is being driven. However, the effect is only to shift the dispersion relation along the frequency-axis does not alter $\left(\frac{d\omega(k)}{dk}\right)$. The relation in Supplementary Figure 9 is obtained under a constant $\mathbf{H}_{so}$ =100 mT. For the calculation of the dispersion relation, we used a shorter computational domain (40000 cells long) due to resulting large file sizes due to fine time sampling. The parameters were: time step = 1 fs and data was recorded every 3 fs during a total time of 50 ps.

Supplementary Note 5

As mentioned in the main text, a different excitation protocol can result in a completely different DW distribution. Supplementary Figure 10 shows another such protocol.

Supplementary Note 6

The dampening process of the oscillations (see Supplementary Figure 11 and its caption) can be mapped into damped harmonic oscillator reproducing nicely the convoluted oscillations obtained from numerical simulations.

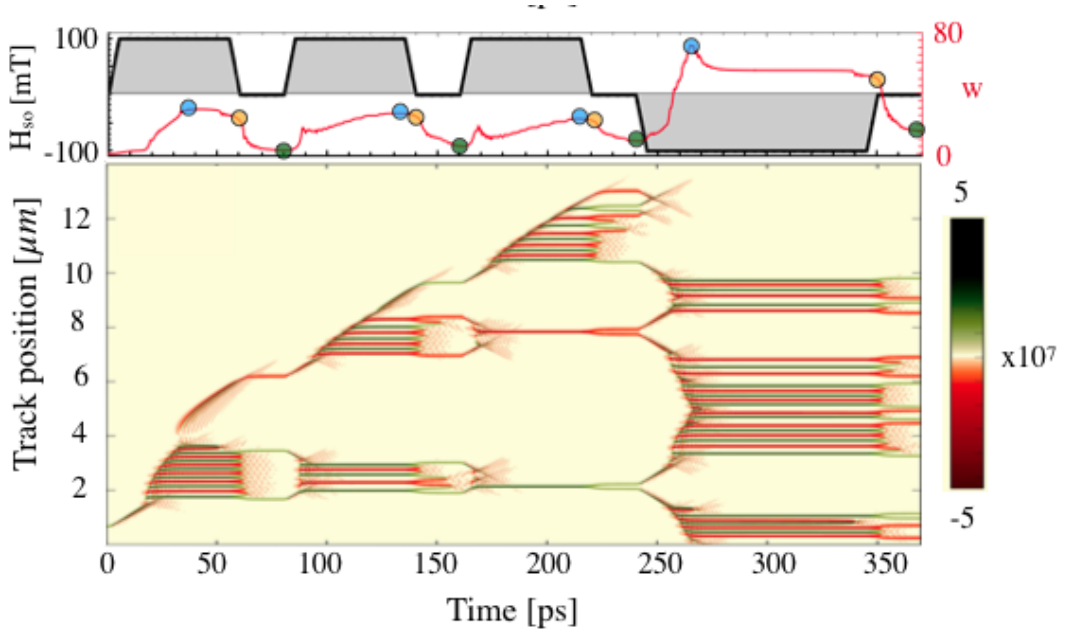

Supplementary Figure 10: Top: an excitation protocol consisting of three positive pulses and one long negative pulse. Bottom, the winding number density versus space and time

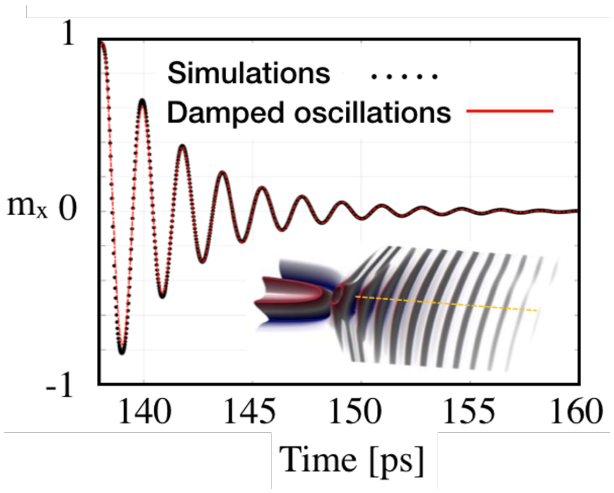

Supplementary Figure 11: Time evolution of the m_x-component at a fixed point X_0 of annihilation, extracted along the (X_0,t) line shown by the dotted yellow line in the inset. The oscillations are well fitted by a function y=Exp(-bt)[A*cos(ωt-ϕ)], thus verifying the exponential decay in Eq. 30

Supplementary References

1- Konstantin Guslienko, Ki-Suk Lee & Sang-Koog Kim. *Dynamic Origin of Vortex Core Switching in Soft Magnetic Nanodots.* Physical Review Letters **100**, 027203, 2008.
2- John R: Klauder *Path integrals and stationary-phase approximations.* Phys. Rev. D **19**, 2349, 1979.
3- Michael Stone. *Magnus force on skyrmions in ferromagnets and quantum Hall systems.* Phys. Rev. B **53**, 16573, 1996.
4- Konstantin Guslienko *Gauge and emergent electromagnetic fields for moving magnetic topological solitons.* Euro. Phys. Lett. **113**, 67002, 2016.
5- GRADSHTEYN, Izrail Solomonovich; RYZHIK, Iosif Moiseevich. *Table of Integrals, Series, and Products.* Academic Press, 2014.